Nonequilibrium Laser-Based Synthesis of Nanoparticle Ensembles

by

Salah Elafandi

A thesis submitted to the Graduate Faculty of
Auburn University
in partial fulfillment of the
requirements for the Degree of
Master of Science

Auburn, Alabama
Dec 12, 2020

Keywords: 2D materials; 2D nanoparticles; 2D quantum dots; laser ablation; laser-based synthesis

Approved by

Masoud Mahjouri-Samani, Chair, Assistant Professor of Electrical and Computer Engineering
Robert N. Dean, McWane Professor of Electrical and Computer Engineering
Peng Li, Assistant Professor of Electrical and Computer Engineering

Abstract

Two-dimensional (2D) materials have grabbed tremendous interest in the recent years because of their exotic electrical and optical properties, which make them potential candidates for next-generation electronics and optoelectronics. Further confining of these 2D materials laterally forms zero-dimensional (0D) nanoparticles that imitate the interesting characteristics of quantum dots (QDs). In this thesis, I am reporting a laser-based method to produce nanoparticle ensembles derived from 2D materials in a solution-free, fast, and effective fashion. This method has the potential of forming digital heterostructures of nanoparticles, which are then post-heated to crystallize. Scanning electron microscopy (SEM) with energy dispersive X-ray (EDS), transmission electron microscopy (TEM), and optical microscopy have been used to investigate the morphology and structural compositions of the obtained depositions. In addition, the photoluminescence (PL) spectroscopy, Raman spectroscopy, and time-correlated single-photon counting (TCSPC) system were used to investigate the electronic and optical properties of obtained samples as a function of the growth parameters.

Acknowledgments

I would like to thank Dr. Masoud Mahjouri-Samani for his continuous mentoring and guidance during my master's degree. He taught me many scientific concepts and how to be a better researcher. In addition, I would like to thank Dr. Baha Yakupoglu for his mentorship, guidance and training during my first year at Auburn. His training was crucial to my program and progress. In addition, he was like an older and more experienced brother who supported and advised me on professional and personal levels. Furthermore, I would like to appreciate my lab-mates, Nurul Azam and Zabihollah Ahmadi, collaboration on many research projects and taking part in research discussions with me.

I would like to thank Dr. Robert Dean for accepting to be a member of my thesis defense committee, and for his valuable advices. In addition, his classes on solid-state sensors and photovoltaics were some of the most interesting, informative and enjoyable classes. I would also like to thank Dr. Peng Li for his willingness to be part of my defense committee and his encouraging comments and advices.

I would also like to thank Dr. Mandoye Ndoye, Dr. Arbin Ebrahim, Dr. Channa S. Prakash, Dr. Prakash C. Sharma and Dr. Akshaya Kumar for their support and advising during my undergraduate's years, and beyond.

In addition, I would like to express my deep gratitude to my parents, Dr. Gamal Elafandi and Souzan Baioumy, for their lifetime support, love, encouragement, engagement, and commitment. Without them, I would not have been the person I am today.

Last but not least, I would like to thank my wife, Salma Mansour, who brought extra happiness and love to my life, and filled a big emotional gap in my life. Since she entered my life,

she has always stayed by my side, in ups and downs. She is always there to listen to me and cheer me up whenever needed.

Table of Contents

List of Tables

List of Figures

List of Abbreviations

0D	Zero-dimensional
2D	Two-dimensional
FWHM	Full width at half maximum
GaSe	Gallium Selenide
In_2Se_3	Indium (III) Selenide
PL	Photoluminescence
PLD	Pulsed Laser Deposition
QDs	Quantum Dots
SEM	Scanning electron microscopy
TEM	Transmission electron microscopy
TCSPC	Time-correlated single-photon counting

Chapter 1

Introduction

Since graphene was discovered in 2004, a collection of novel two-dimensional (2D) materials have been discovered and intensively investigated [1-3]. Notable examples of such ultra-thin materials include hexagonal boron nitride (hBN) [4], metal chalcogenides (MCs: e.g., GaSe, InS) [5] and transition metal dichalcogenides (TMDCs: e.g., MoS_2, WSe_2) [6, 7]. These single-layered materials family have given rise to state-of-art electrical [7-9], optical [10], chemical [11], and mechanical [12] properties. The structural and quantum confinement of these layered materials to the 2D plane is often the driving-force of such properties [13-15]. In conclusion, 2D materials are deemed as revolutionary compliments or alternatives of conventional 3D electronic and optoelectronic materials [16-18].

Additional confining of these 2D materials laterally yields zero-dimensional (0D) nanoparticles that imitate the exotic characteristics of quantum dots (QDs) [19-21]. Such nanoparticles derived from 2D materials show enhanced and novel properties compared to their parent 2D materials [22, 23]. These advantages and novel properties include tunable luminescence [24-26], higher specific surface area [27, 28], ability to hybridize with other nanomaterials [29, 30], low toxicity [31], improved dispersibility in both aqueous and nonaqueous solvents [32, 33], in addition to doping and functionalization flexibility [34, 35]. Therefore, they are appealing candidates for optical [29], electronic [36], biomedical [25], energy [4], sensing [22], and catalytic [37] applications.

Ultrasonication-based [38, 39], which are usually complemented by solvothermal treatments [40, 41], synthesis methods have been largely utilized to fabricate 2D nanoparticles because of their ability to preserve the inherent characteristics of 2D bulk crystals and low toxicity [42].

However, these methods are not only time-consuming, but also lack repeatability and high quantum and production yields [42]. After that, femtosecond laser ablation in aqueous environment has been adopted as a synthesis method that tackles the disadvantages of ultrasonication-based methods [43, 44], and was viewed as a fast and nonpolluting approach to produce and functionalize 2D QDs [34, 45]. Intercalation-assisted exfoliation was also introduced as an effective technique to obtain large-scale monolayer QDs [36, 46]. However, this technique is limited by the possible phase transitions [47] and contaminations [48] occurring while synthesizing. Electrochemical synthesis [49, 50] has recently been adopted too and achieved high reproducibility in low-cost fashion. In conclusion, these methods have shown great success in obtaining 2D QDs/nanoparticles. However, the absence of compositional tunability in addition to compatibility with the direct deposition and digital formation of heterostructures and hybrid materials are few of the limitations facing these techniques.

In the recent years, the high-pressure pulsed laser deposition (PLD) has emerged as a mean of obtaining metastable nanoparticles in the gas phase [51]. For instance, Mahjouri-Samani et al. have successfully fabricated various metastable nanoparticles and nanosheets using high-pressure PLD [52]. In addition, Dai et al. have also used PLD to deposit CdSe QDs on Zn_2SnO_4 nanowires [53]. Typically, during the PLD process (Figure 1a), ablating a target forms a forward-directed laser-generated plasma which is made up of neutral atoms and fast atoms that are succeeded by slower-moving clusters and molecules [54]. In a vacuum, due to the high kinetic energy of the neutrals and fast ions, dense films are deposited on a substrate. However, to create suitable conditions for nanoparticle formation, elevated background gas pressures are used to condense the plume and moderate the kinetic energies. The correlation between background gas pressures, nanoparticle

formation evolution and laser-generated plume dynamics is simply illustrated in Figure 1b, while other growth conditions (e.g., laser fluence, repetition rate) are sustained.

Here, PLD was used to produce nanoparticle ensembles derived from 2D materials in a solution-free, fast, and effective fashion. The tunability of the PLD, in an argon gas background pressure environment, has allowed us to condense the plume and form stoichiometric aggregates and nanoparticles in the gas phase (for verification, refer to Figure A.1). This approach has the potential to eliminate the current complications of existing methods, such as slowness, toxicity and uncontrollability of chemical reactions. In addition, it has the advantage of assembling digital nanoparticle heterostructures by alternating between different targets. A step of thermal annealing has been used to crystallize the deposited nanoparticles. Scanning electron microscopy (SEM) with energy dispersive X-ray (EDS), transmission electron microscopy (TEM) and optical microscopy have been used to investigate the morphology and structural compositions of the obtained depositions. In addition, photoluminescence (PL) spectroscopy, Raman spectroscopy and time-correlated single-photon counting (TCSPC) system were used to investigate the electronic and optical properties of obtained samples as a function of the growth parameters.

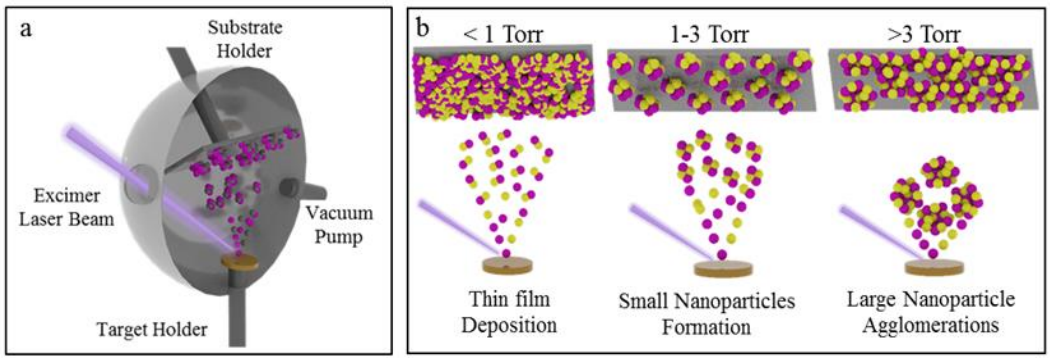

Figure 1.1. (a) Schematic of the pulsed laser deposition (PLD) system used to generate the nanoparticles. (b) Schematic illustration of the plume dynamics and nanoparticles' evolution as a function of background pressure. Reprinted from [55].

Chapter 2

Experimental Methods

Pulsed Laser Deposition: A 21-inch spherical ultra-high vacuum chamber was used to execute these pulsed laser ablation/deposition experiments. A CompexPro (Coherent Inc., Santa Clara, CA, USA) KrF excimer laser with a wavelength of 248 nm and a pulse duration of 20 ns was used to ablate a rotating bulk target ($GaSe/In_2Se_3$) at a 45° angle of incidence. This resulted in a forward-directed laser-generated plasma that contains the nanoparticles which are deposited on a 2 × 2 cm Si/SiO_2 substrate that is located at the tip of the plume parallel to the target. To ensure homogenous and pure collection of nanoparticles, the substrate was located 1-2 cm above the visible plume. In addition, a laser repetition rate of 2 Hz was picked to make the next generated plume arrive after the first plume is cleared and minimize the effect of plume-plume collisions. The laser energy was adjusted to 300 mJ with a beam size of 2 × 5 mm beam size, i.e., 3 $J \cdot cm^{-2}$, to maintain stoichiometric deposition. Finally, up to 5000 laser pulses were used to ablate the target to deposit enough amount of the nanoparticles for successive characterizations.

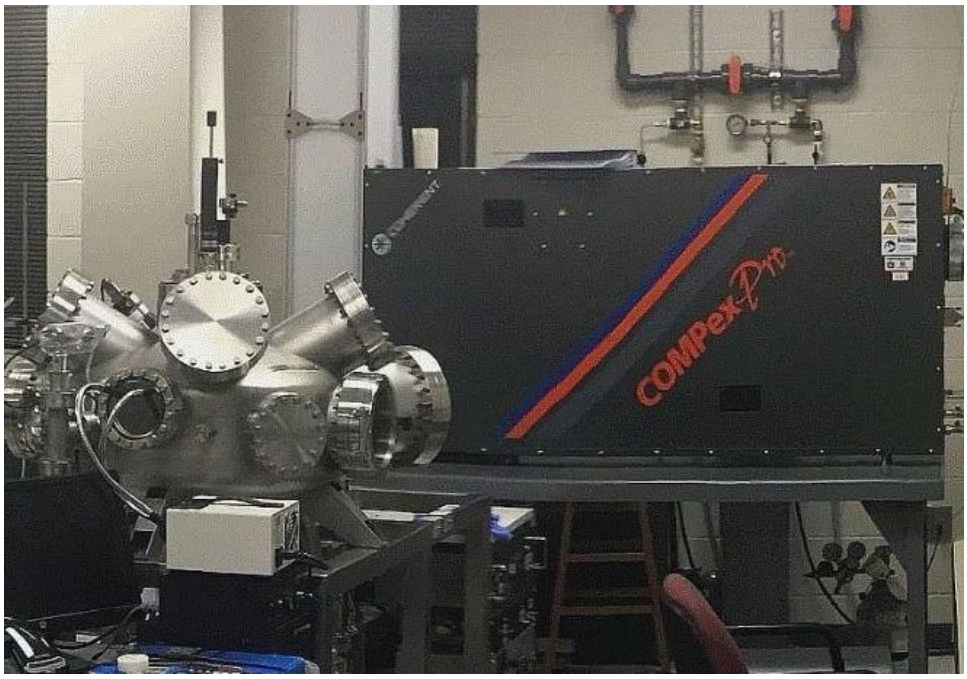

Figure 2.1. Picture of the pulsed laser deposition (PLD) system used in this project. The picture is showing the ultra-high vacuum chamber on the left and the COMPex-Pro excimer laser.

Thermal Annealing: Following deposition, the nanoparticles were thermally annealed in3-inch diameter 3-zone tube furnace. A Si/SiO_2 substrate which contains the deposition on its surface was placed in a ceramic boat and positioned in the center of the furnace's tube. The substrate was then heated in a chemically inert atmospheric pressure environment. To achieve that, the tube was first pumped down to a high vacuum and pumped up again to atmospheric pressure by filling the tube with argon gas. To avoid oxidation and maintain an inert environment, a continuous flow of 100 sccm argon gas was maintained during heating and cooling down to room temperature.

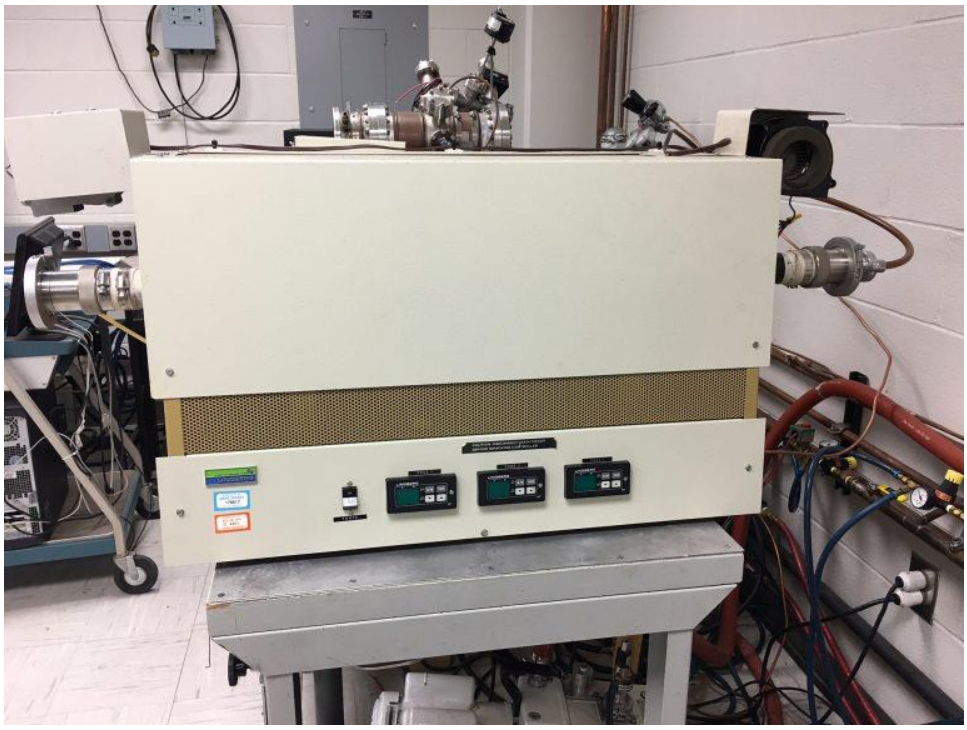

Figure 2.2. The three-zone tube furnace that is used for thermal treatments.

Optical Spectroscopy: Photoluminescence, Raman and PL decay lifetime measurements were performed using a custom-made optical spectroscopy system. The characterizations were executed using excitation sources of a picosecond 405 nm and a continuous-wave 532 nm lasers that are passing through a 50× objective lens with a numerical aperture of 0.75. A fully automated Horiba iHR spectrometer (HORIBA Scientific, Piscataway, NJ, USA) with a triple grating turret was used. For PL analyses, a 300 g/mm grating was used, while a 1200 g/mm grating was used for Raman analyses. In both Raman and PL analyses, the laser exposure was minimized to avoid potential beam-induced oxidation or sintering. Finally, the PL decay lifetime measurements were performed using a picosecond 405 nm laser as the excitation source. A Horiba time-correlated single-photon counting (TCSPC) system along with Horiba EzTime Software (HORIBA Scientific, Piscataway, NJ, USA) was used to obtain and analyze the PL decay lifetime measurements data. To minimize oxidation and sintering of the nanoparticles, the number of counts was limited to 1000 counts.

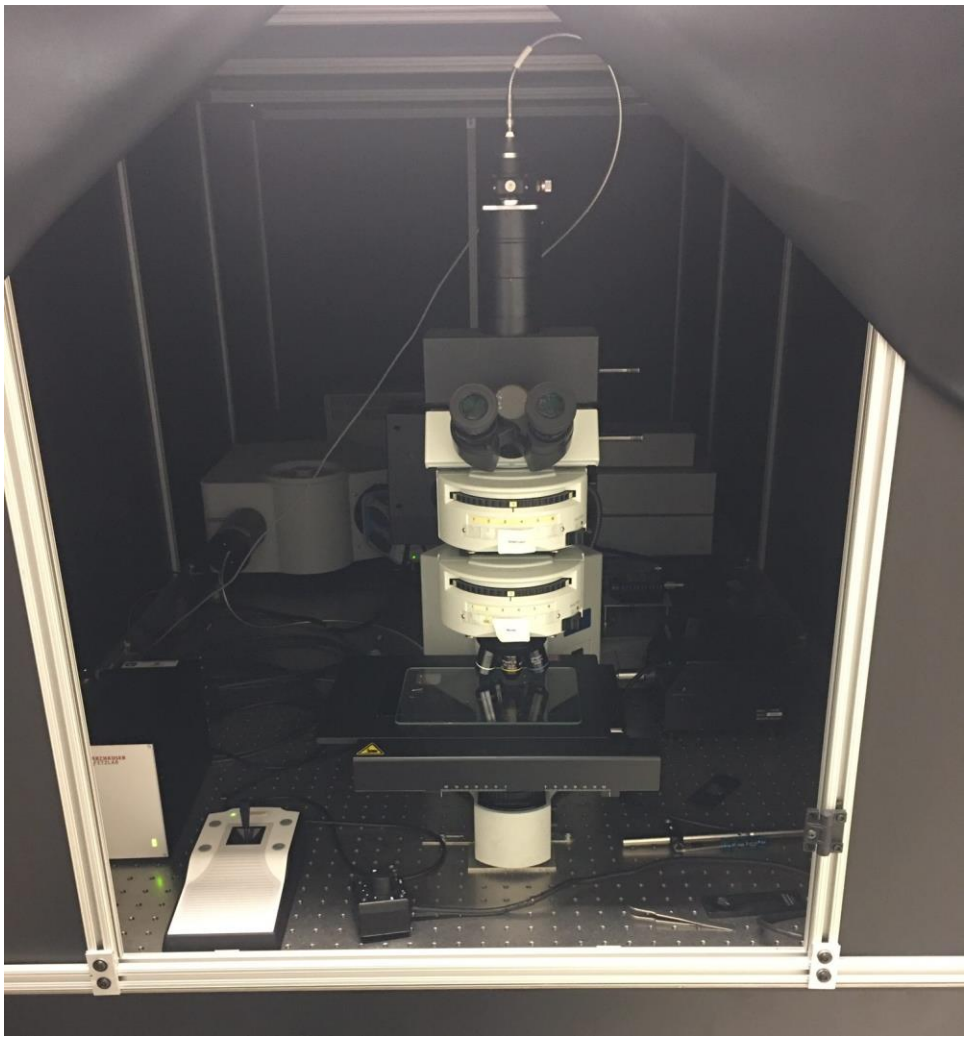

Figure 2.3. The optical spectroscopy system that is used for Raman, photoluminescence and TCSPC analyses.

Electron Microscopy: A high-resolution Zeiss EVO 50 variable pressure scanning electron microscope (SEM) (Carl Zeiss Microscopy LLC, White Plains, NY, USA) with digital imaging and Oxford Instruments INCA spectrometer for energy-dispersive X-ray spectroscopy (EDS) (Oxford Instruments NanoAnalysis, Concord, MA, USA) was used to analyze the topography and structural composition of the deposited samples. While 10 kV accelerating voltage was used for SEM analyses, EDS analyses were performed using a 20 kV accelerating voltage. Oxford INCA software (Oxford Instruments NanoAnalysis, Concord, MA, USA) was used to analyze the EDS data. In addition, a Zeiss EM10 transmission electron microscope (TEM) (Carl Zeiss Microscopy

LLC, White Plains, NY, USA) was used to characterize single-particle and aggregation. An accelerating voltage of 60 kV was used for TEM analyses. To prepare the TEM grids, the samples were sonicated in ethanol for 1 min to detach the particles from the substrate. Then, the TEM grids were stirred inside the solution to collect the nanoparticles.

Figure 2.4. The SEM system that is used to analyze the topography and structural composition of the deposited samples.

Figure 2.5. The TEM that is used to characterize single-particle and aggregation.

Chapter 3

Highly Luminescent Gallium Selenide Nanoparticles

The first synthesized material is gallium selenide (GaSe) which is an interesting 2D material with a direct bandgap of approximately 2.2 eV in its bulk form. In addition, it has a D_{3h} symmetry with a lattice constant of 0.374 nm [54]. GaSe nanoparticles have been first synthesized in 1996 when Stoll et al. used metal–organic chemical vapor deposition (MOCVD) to produce "strings of pearls"-shaped nanoparticles with a mean diameter of 42 nm [56]. A year later, Allakhverdiev et al. ultrasonicated a bulk GaSe crystal in methanol to produce colloidal GaSe [57]. Finally, In 2001, highly confined and luminescent surface-capped GaSe nanoparticles were produced using a high-temperature inorganic synthesis combined with column chromatography by Chikan and Kelly [58].

To condense the plume and form nanoparticles, argon gas was used to adjust the background gas from 0.5 to 5 torr. Tuning the background pressure within this range has allowed us to form structures ranging from dense films to mesoporous structures as a function of elevated pressure. The SEM images of the samples deposited at background pressures of 0.5, 2, and 5 torr, in the as-deposited case, are shown in Figure 3.1a, d, and g, respectively. Using a pressure up to 0.5 torr (Figure 3.1a), the resulted deposition has a minimum number of nanoparticles and consists mainly of a dense film due to the high kinetic of the smaller aggregates, molecules and atoms within the plume. In addition, as shown in Figure 3.1d, increasing the pressure up to 2 torr resulted in condensation of the plume to a semi-sphere with a diameter of 5 cm which formed nanoparticles that deposited mesoporous structures onto the substrate. Further increasing the pressure up to 5 torr (Figure 3.1g) resulted in loosely connected and fluffier depositions onto the substrate as a result of the partially crystallized and sintered nanoparticle agglomerations. The cause of this

crystallization and sintering effects is the severe condensation of the plume to a semi-sphere shape with a diameter of about 1.5 cm. Finally, it was very challenging to deposit samples using pressures above 5 torr due to the small size of the plume. In conclusion, the size and density of the nanoparticle agglomerations were observed to be directly correlated to the condensation dynamics induced by background pressure.

To reduce defects and surface traps of the nanoparticles, they were baked at a baking range of 200 to 500 °C in atmospheric pressure. The heat-treatments were executed in a 3-zone tube furnace for 30 minutes, while maintaining a continuous flow of argon during the heating and cooling processes to avoid oxidation. The SEM images shown in Figure 3.1b and c are showing the effects of baking 0.5 torr samples at 300 and 500 °C are shown in Figure 3.1b and c. As 0.5 torr samples are mainly consisting of nearly continuous dense structures, the effects of baking the nanoparticles lack significant morphological changes. On the other hand, the SEM images showing the effects of baking 2 torr at 300 and 500 °C are shown in Figure 3.1e and f, while the effects of baking 5 torr samples at 300 and 500 °C are shown in Figure 3.1h and i. As seen from the SEM images, increasing the temperatures results in increased nanoparticles sintering and larger nanoparticle agglomerations and pores formation.

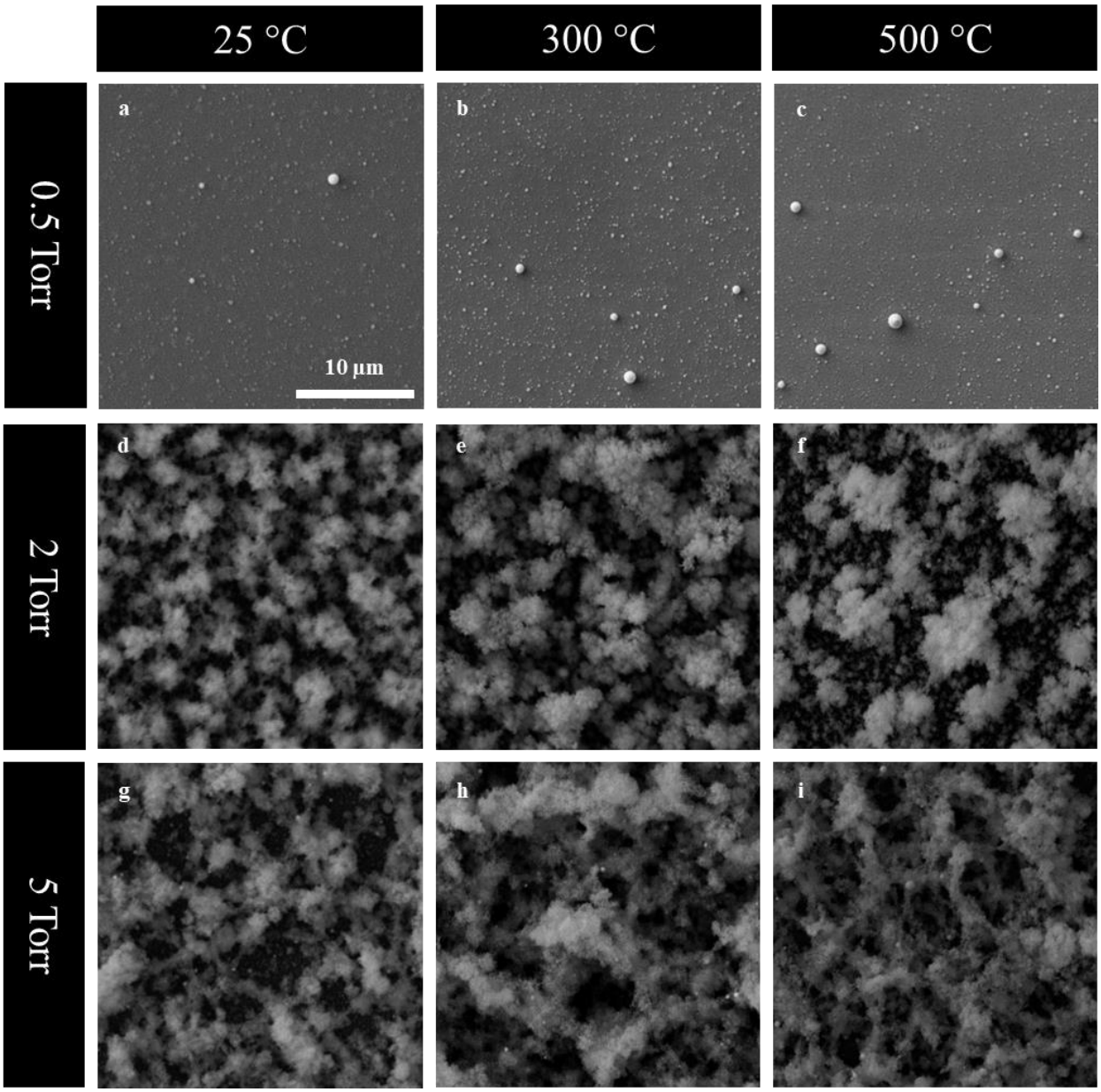

Figure 3.1. Scanning electron microscopy (SEM) images of GaSe samples deposited at 0.5 (a, b and c), 2 (d, e and f), and 5 torr (g, h and i) background pressures in the as-deposited case (a, d and g) and baking temperatures of 300 °C (b, e and h), 500 °C (c, f and i). While 0.5 torr samples show dense structures, the 2 and 5 torr samples show mesoporous structures as an indication of nanoparticles formation. Baking the samples causes the sintering of the nanoparticles and larger nanoparticle agglomerations. All shown images are on the same scale bar.

TEM imaging was used to characterize the nanoparticle aggregates and the structural evolution of 2 torr samples in the as-deposited case as well as at different crystallization temperatures. The samples were sonicated in ethanol for 1 min to detach the particles from the

substrate, and the TEM grids were stirred inside the solution to collect the nanoparticles. As shown in Figure 3.2a, the as-deposited samples consisted of separable 5-10 nm individual nanoparticles. When these depositions were baked at 300 °C (Figure 3.2b), partially crystallized and sintered nanoparticles were obtained. Further sintering and crystallization took place when the nanoparticles were baked at 500 °C (Figure 3.2c), leading to larger agglomerations. In conclusion, these findings are in agreement with the SEM analyses.

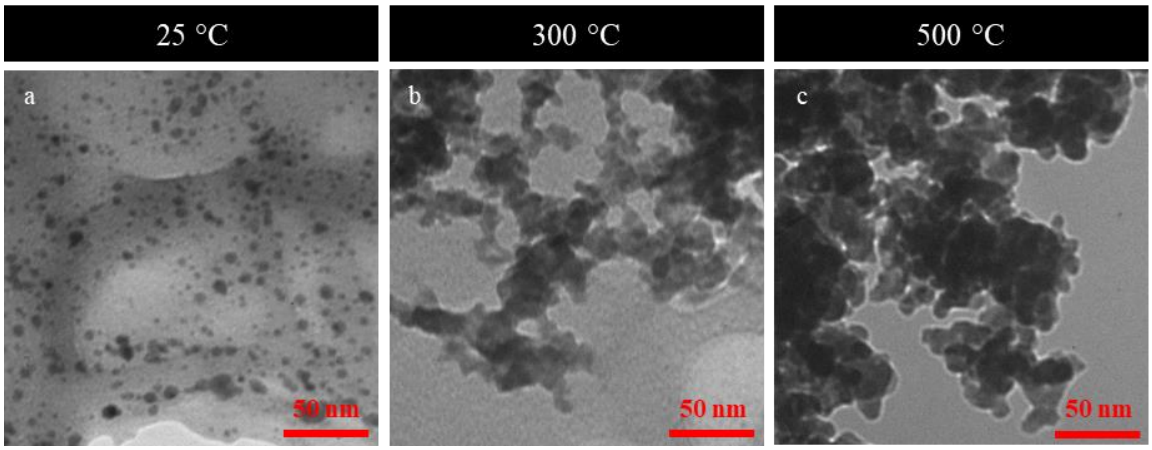

Figure 3.2. Transmission electron microscopy (TEM) images showing the morphology of the (a) as-deposited 2 torr sample and the effect of baking temperatures (b) 300 °C and (c) 500 °C on it. The TEM image in the as-deposited sample is showing that it consists of separable nanoparticles. However, baking them at higher temperatures cause further sintering of the particles.

To correlate the electronic and optical properties of the deposited nanoparticles to growth conditions, i.e., background pressures and crystallization temperatures, photoluminescence spectroscopy (PL) and time-correlated single-photon counting (TCSPC) system were used. The PL spectra and PL decay lifetime measurements were obtained using a picosecond 405 nm as an excitation source. By lowering laser powers and acquisition times, the exposure of the samples to lasers was minimized, and possible laser-induced alterations, such as photo-oxidation or additional sintering and crystallization, were avoided. Horiba EzTime software (HORIBA Scientific, Piscataway, NJ, USA) was used to fit the PL decay lifetime curves. These curves were fitted using a tri-exponential function and characteristic lifetimes were successfully obtained (the fitting

parameters are shown in Table A.3-7). The correlation between PL emissions and background pressures (0.5, 1, 2, 3, and 5 torr) in the room-temperature case and at the indicated baking temperatures (200, 300, 400, and 500 °C for 30 min) are shown in Figure 3.3a-e. In addition, the corresponding PL lifetime decay measurements are shown in Figure 3.3f-j.

Three observations could be seen from correlating the background pressures to PL emissions and PL lifetime decay measurements of the deposited nanoparticles. The first observation is the strong PL emissions from the as-deposited nanoparticles (Figure 3.3a), which are mainly amorphous. Compared to the 625 nm central emission of bulk GaSe crystal (Figure A.2), the nanoparticles showed considerable blue-shifted central emission of approximately 540 nm (for central emission values, refer to Table A.1). In the as-deposited case, the sample deposited at 0.5 torr showed the weakest intensity because of the dominance of dense film structures on the substrate. However, when nanoparticles started forming at higher pressures, the intensity values started increasing, with nanoparticles deposited at 2 torr showing the maximum intensity. This nanoparticles formation has also led the average lifetime of the room temperature-deposited samples (Figure 3.3f) to gradually increase up to 2 torr and then slightly decrease afterward.

The second observation is that baking the samples up to 300°C, the PL (Figure 3.3b and c) witnessed minimal full width at half maximum (FWHM) widening (for FWHM values, refer to Table A.2) and red-shifting. In addition, the PL decay lifetimes (Figure 3.3g and h) generally increased as the deposition background pressure increased as crystallization is mainly dominating at these temperatures, while sintering is still minimum. However, baking the samples at higher temperatures (Figure 3.3d and e), notable FWHM widening was recorded and the central emission red-shifted significantly closer to the central emission of bulk GaSe, and even beyond that. In addition, the lifetimes (Figure 3.3i and j) decreased again. Such behavior could be because

sintering starts dominating over crystallization, which is deleterious to the quantum confinement of the nanoparticles.

Third, the samples deposited at lower background pressures witnessed significant red-shifting and broadening at a faster rate compared to the nanoparticles deposited at higher pressures. For instance, 0.5 and 1 torr samples started widening and red-shifting at approximately 300 °C (Figure 3.3c), while the higher-pressure samples showed such significant widening and red-shifting at 400 °C (Figure 3.3d) only. This is because high-pressure samples encounter partial crystallization during deposition, which makes them less sensitive to low-baking temperatures. Therefore, low-pressure samples tend to crystallize faster at lower temperatures, and higher temperatures cause further sintering of the nanoparticles, which deteriorate the quantum confinement and increase the particle size distribution. Finally, it should be noted that 0.5 and 1 torr samples exhibited unstable and random PL emissions at higher temperatures (e.g., 400–500 °C), but this could be attributed to their thin-film like morphology or a specific phase transition taking place.

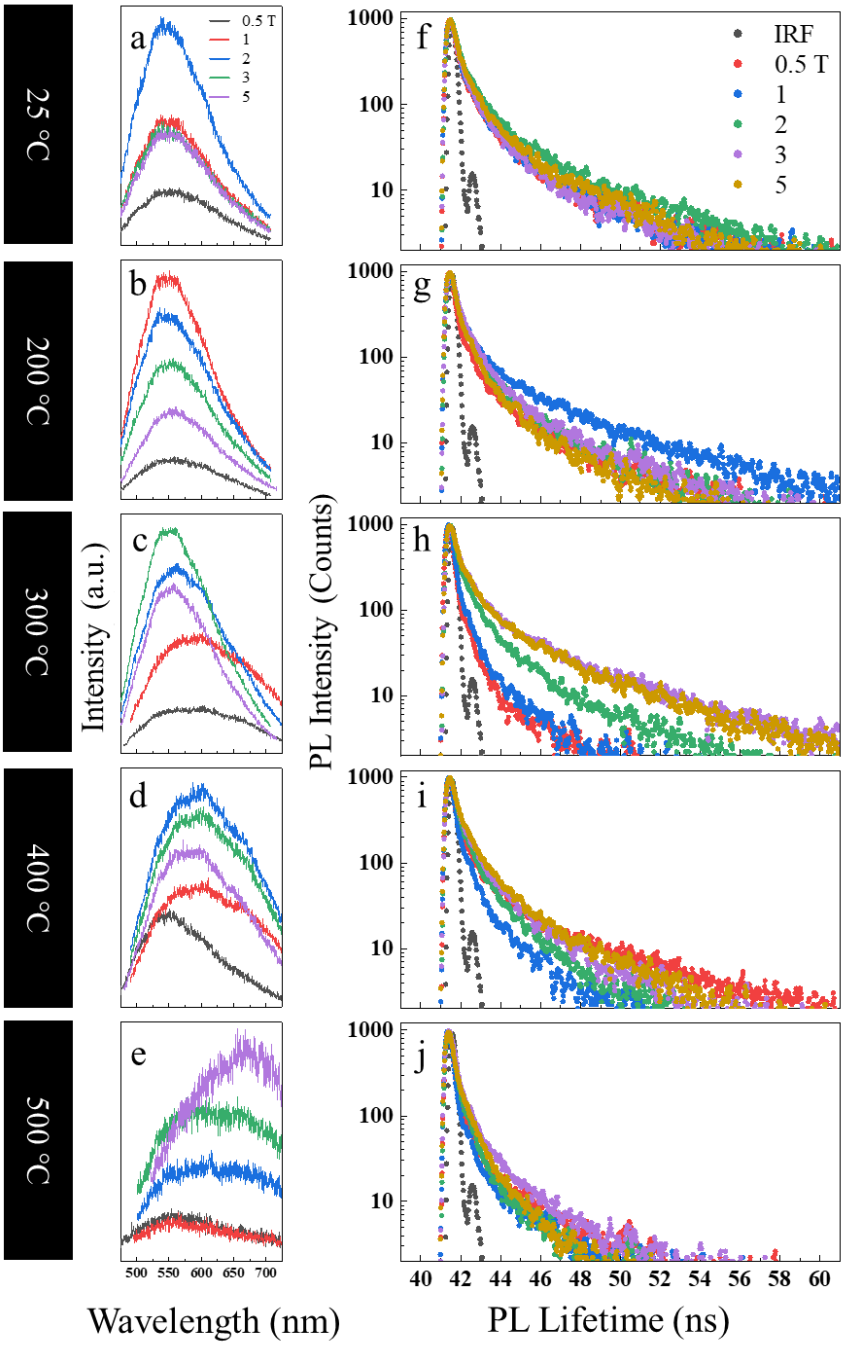

Figure 3.3. PL spectra of the GaSe samples that were deposited at various pressures for the as-deposited case (a) and at the indicated baking temperatures (b–e). The weakest PL is recorded by 0.5 torr samples due to the formation of dense films (i.e., no nanoparticles). As nanoparticles start forming at higher pressures, intensities are increased. PL decay lifetimes curves of the GaSe samples that were deposited at various pressures for the as-deposited case (f) and at the indicated baking temperatures (g-j). The general trend is that the PL lifetime increases as a function of increasing deposition pressures.

In addition, for better visualization of the effect of baking temperature on 0.5, 1, 2, 3, and 5 torr samples on the PL and PL decay lifetimes, the data are also replotted in Figure 3.4a–j. As shown in Figure 3.4c, d and e, the PL emissions of the nanoparticles deposited at pressures of 2, 3, and 5 torr have slightly red-shifted and broadened. In addition, their intensity values have significantly increased up to 300 °C. However, further baking at higher temperatures (i.e., 400 and 500 °C) has led to a steady reduction in intensity values as well as significant FWHM broadening and red-shifting. Such a trend is due to the crystallization effect dominating over the effect of nanoparticles sintering at low baking temperatures (i.e., 200 and 300 °C) which enhance the intensity values while maintaining minimum FWHM widening and central emission's red-shifting. However, at higher baking temperatures (i.e., 400 and 500 °C), nanoparticles sintering takes place at higher rates causing significant FWHM broadening, red-shifting, and deterioration of the intensity values due to the formation of random particles size distributions and new defects.

The replotted PL decay lifetimes are shown in Figure 3.4f-j. In general, the PL decay lifetimes were in agreement with the PL emissions, and have even provided more information about the electronic and optical properties. For instance, as shown in Figure 3.4g, the average lifetime of the as-deposited 1 torr sample has gradually increased from 0.313 ns to 0.319 ns when it was baked at 200 °C. After that, the average lifetime has significantly dropped at higher baking temperatures. This trend is agreeing well with the PL analyses. As mentioned before, baking the samples lead to two results, namely crystallization and sintering. Baking the 1 torr sample to 200 °C has caused a reduction in the defects, which increased the lifetime. However, at higher baking temperatures, the sintering took place at higher rates, dominating over crystallization, forming new defects and random particle size distribution, and consequently reducing the average lifetime. In the case of 2 torr samples (Figure 3.4h), a gradual decrease in the average lifetime has been observed. This is a

slightly different case than 1 torr, as sintering and crystallization taking place at comparable rates. This is causing a reduction in shallow and deep defects due to crystallization. However, nanoparticles' sintering is also causing random particles size distribution and forming new defects. Therefore, the final result of these competing mechanisms is only a gradual/slight decrease in the average lifetime as baking temperatures increase.

The average lifetimes of 3 torr samples, shown in Figure 3.4i, have gradually increased up to 300 °C, slightly decreased at 400 °C, and finally significantly dropped at 500 °C. In the case of 3 torr, low baking temperatures have crystallized the samples, reducing deep and shallow defects, with lower rates of sintering compared to lower pressure samples. Therefore, an increased average lifetime has been observed. However, at higher temperatures sintering started dominating over crystallization, and the average lifetime has decreased. A similar case has been the samples deposited at a background pressure of 5 torr (Figure 3.4j), except that the average lifetime of the sample baked at 200 °C has decreased compared to room-temperature one.

In conclusion, there are a few competing mechanisms when baking the samples. First, baking the samples crystallizes them, reducing deep and shallow defects as well. However, the reduction of deep defects increases the average lifetime of the samples but the reduction in shallow defects decreases the average lifetime [59]. On the other hand, baking the samples lead to nanoparticles' sintering, which creates new defects, and consequently decreases the lifetime. In addition, the density and partial crystallization of the nanoparticles at each deposition pressure play a key role. For instance, at baking temperatures up to approximately 300 °C, the samples tend to crystallize, while sintering is still minimum. However, higher sintering rates take place at high baking temperatures, dominating over the effect of crystallization, and also forming increased particle size distributions and defects.

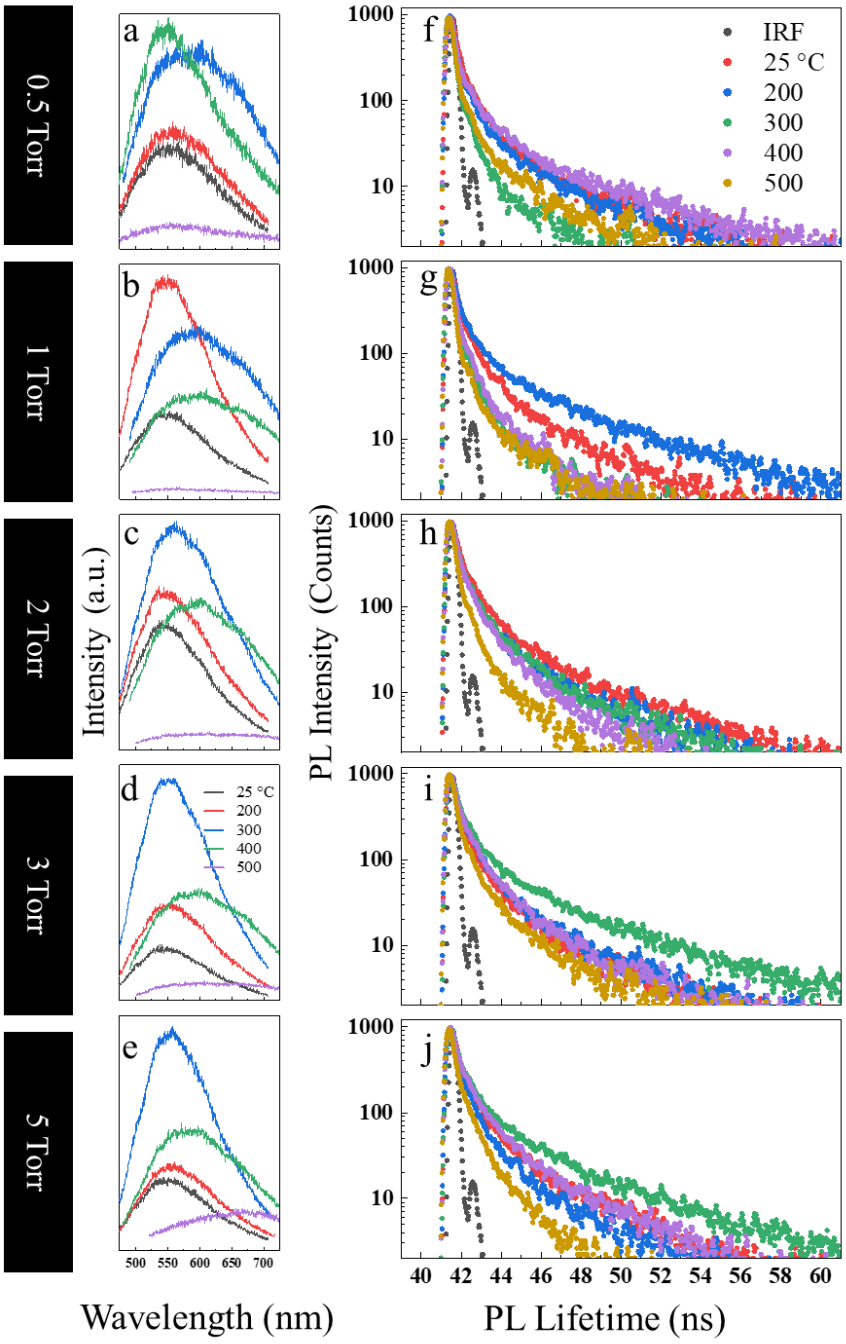

Figure 3.4. PL spectra showing the effect of baking temperature on the samples deposited at 0.5 (a), 1 (b), 2 (c), 3 (d) and 5 torr (e) background pressures. The nanoparticle emission increases up to a baking temperature of approximately 200–300 °C. However, further sintering takes place at higher temperatures, leading to reduced intestines. PL decay lifetime curves showing the effect of baking temperature on the samples deposited at 0.5 (f), 1 (g), 2 (h), 3 (i) and 5 torr (j) background pressures. The overall trend shows that the PL lifetime decreases as the baking temperature increases.

Finally, to get an idea about the effect of baking time on PL emission and PL decay lifetime of the nanoparticles, the 2 torr sample was baked at 300°C, since this condition has significantly increased the emission intensity with minimal FWHM broadening, for 1, 15, 30, and 120 min. As shown in Figure 3.5a, a significant PL intensity enhancement accompanied by gradual FWHM broadening was observed. In addition, the average PL lifetime (Figure 3.5b and c), the average lifetime has significantly decreased up to a baking time of 30 minutes, as a result of the reduction in shallow traps, and probably gradual sintering too. However, with longer baking times (i.e., 120 min), the average lifetime increased again due to the domination of crystallization and reduction of defects.

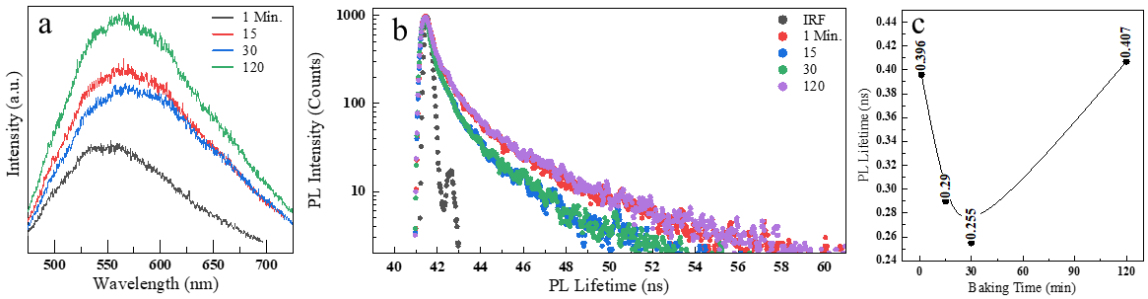

Figure 3.5. (a) PL, (b) PL decay lifetime curves and (c) average PL lifetime of the 2 torr samples baked at 300 °C for different baking times. As the baking time increase, crystallization starts dominating over sintering.

Chapter 4

Multi-Phase Indium (III) Selenide Nanoparticles

Indium (III) selenide is another interesting semiconducting polymorphic 2D material that exists in at least five different crystal phases, namely γ, α, δ, β, κ or a combination of them [60]. Both the defective wurtzite structure (γ) and the hexagonal layered structure (α) are the most stable phases at room temperature [61]. In addition, the β phase is a metastable phase with a similar hexagonal structure to α. However, the outer Se atoms in the α phase are aligned, but in the β phase, they are occupying the Se atoms interstitial sites in the neighboring layers [62]. Therefore, it is challenging to grow single-phase In_2Se_3 [63]. Even after growth, identifying the obtained phase is an arduous job [64, 65]. However, In_2Se_3 has several distinctive properties, such as polymorphism [66], tunable direct and indirect bandgaps [67], high photoresponsivity [68], high absorption coefficient [69], broadband absorption in the visible and near infra-red regions [70], high mobility [71] and current density [72], ferroelectricity [73] and piezoelectricity [74], that make it a promising material for optoelectronics [75], photovoltaic devices [76], phase change memory [77], ferroelectrics [78], piezoelectric devices [74] and ionic batteries [79].

In 2011, Tan et al. reported for the first time the syntheses of γ-In_2Se_3 flowerlike microparticles solvothermally in the presence of biodegradable ascorbic acid as a reducing and capping agent [80]. In addition, Malik et al, have used [$In(^1Pr_2PSe_2)_3$] as a single precursor to obtain In_2Se_3 nanoparticles with an average size of 5.0 ± 1.2 nm through the thermolysis of the precursor 270°C in HDA/TOP system [81]. Liu et al. have also adopted a facile and controllable hydrothermal approach to synthesize In_2Se_3 hollow nanospheres with ethylenediamine (en) as a ligand [82]. Moreover, another one-step mild solvothermal approach was used to obtain flowerlike α-In_2Se_3 nanostructures, that consist of two-dimensional nanosheets using a single solvent of

green, phosphine-free oleic acid (OA) [83]. Botcha et al. have also produced In_2Se_3 nanoparticles with various morphologies and three-dimensional (3D) rod-like flower-shaped In_2Se_3 structures using a single step physical vapor deposition (PVD) [84]. More recently, a pulsed laser ablation in water has been reported by Dhongade et al. to synthesize In_2Se_3 nanocubes with superior field emission characteristics to serve as high current density cold cathode materials [72].

Using or novel laser-based synthesis technique, In_2Se_3 nanoparticles have been produced. As we expected the morphology of obtained In_2Se_3 samples to be similar to GaSe nanoparticles, optical microscopy has been used to ensure such an assumption is still maintained in the In_2Se_3 case. The optical images of the obtained samples are shown in Figure 4.1. Firstly, in the as-deposited case, the 0.5 torr sample (Figure 4.1a) has a low density of nanoparticles and the deposition is consisted of dense films mainly. However, when increasing the pressure up to 2 torr (Figure 4.1b), further condensation of the plume is achieved, and nanoparticulate deposition is obtained. At 5 torr (Figure 4.1c), a fluffier and larger depositions were produced. Baking the samples up to 500 °C (Figure 4.1d-i), the nanoparticles gradually sintered into larger agglomerations and loosely connected networks. In conclusion, up to 500 °C, the samples followed morphology changes similar to the GaSe nanoparticles, as expected.

Interestingly, when the samples were baked at 600 °C (Figure 4.1j, k and l), part of the nanoparticles sintered into nanorods or nanowire-like structures. Although the cause of such transformation is currently unknown, such transformation is especially interesting since most of (or all, to the best of my knowledge) the reported methods of synthesizing In_2Se_3 nanowires or nanorods require the presence of metal catalysts during the process. By observing the cases of 0.5 and 2 torr samples (Figure 4.1j and k), that have a combination of nanoparticles and nanorods, it could be concluded that not all nanoparticles are transitioned into nanorods structures. However,

nanorods are predominantly covering the surface of the 5 torr sample (Figure 4.1l). The number of transformed nanoparticles could be attributed to either amount of the nanoparticles contained on the surface of the substrate or the reactivity and sintering ability of the nanoparticles at every specific pressure.

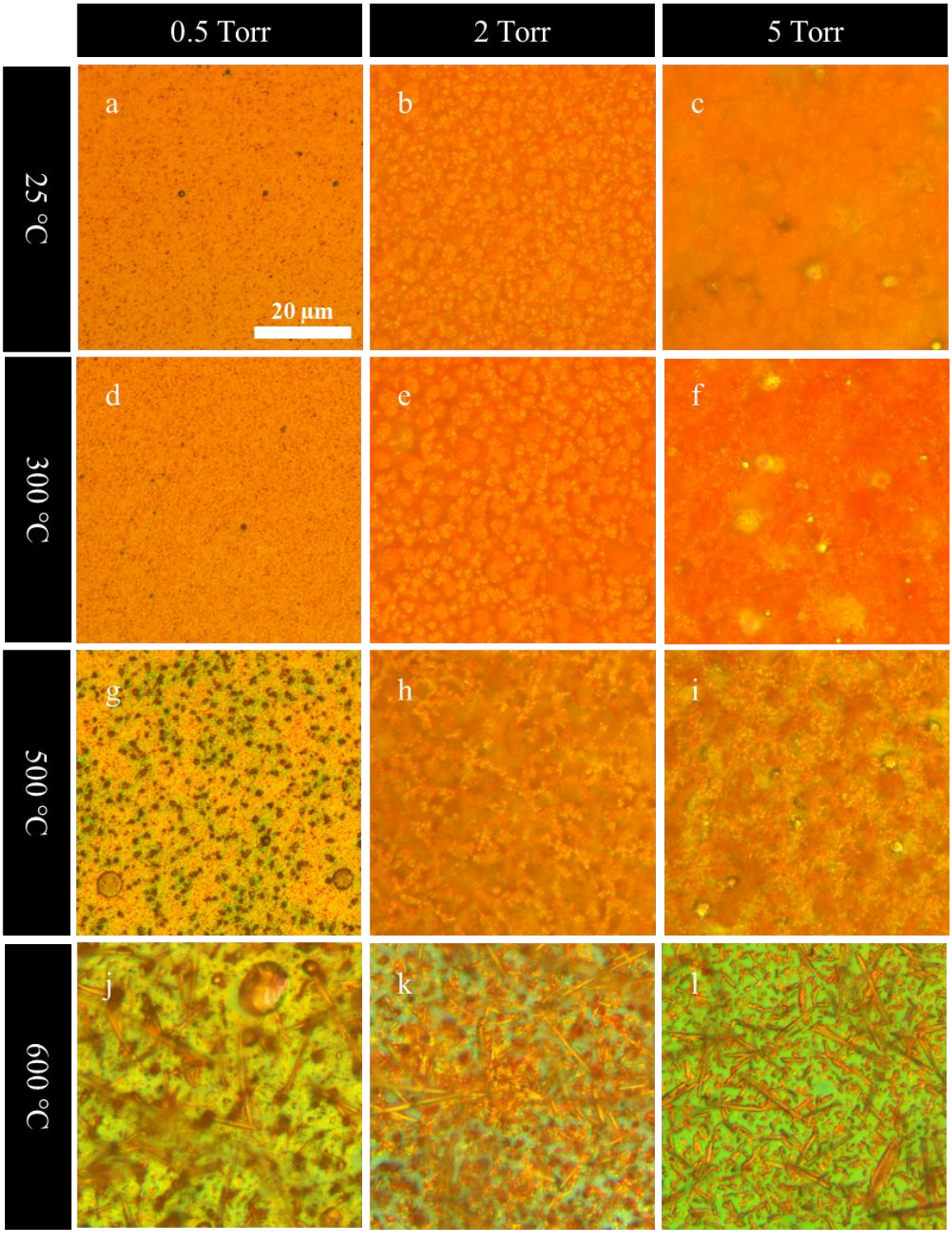

Figure 4.1. Optical images of In_2Se_3 samples deposited at 0.5 (a, d, g and j), 2(b, e, h and k), and 5 torr (c, f, i and l) background pressures in the as-deposited case (a-c) and baking temperatures of 300 °C (d–f), 500 °C (g–i), and 600 °C (j–l). Similar morphology changes up to 500 C, and then an interesting transformation to nanorods at 600C. All images are on the same scale bar.

The samples have been characterized using Raman spectroscopy as well to investigate their structural properties. The samples were excited using a continuous-wave 532 nm laser, and the exposure to the laser was minimized to eliminate photooxidation or sintering. The effects of baking temperatures on 0.5, 1, 2, 3 and 5 torr samples are shown in Figure 4.2a-e. First, the as-deposited samples are showing a very broad peak that is spanning from ~100-250 cm^{-1}. This broad peak could be attributed to the amorphousness of the deposition or due to the contribution of different In_2Se_3 phases. Such characteristic has been maintained even when baking the samples up to 400 °C, although the edges of the Raman bands appeared slightly sharper. When the samples were baked at 500 °C, the Raman spectrum of 0.5 torr sample (Figure 4.2a) indicates a Raman peak located at ~150 cm^{-1} in addition to a narrower and smaller peak at ~116 cm^{-1}, while the red-side shoulders of the 150 cm^{-1} disappear. The 150 cm^{-1} Raman band is a characteristic mode of γ-In_2Se_3 [85, 86], while the 116 cm^{-1} is in the proximity range to A_1 (LO + TO) mode of β-In_2Se_3 [71, 87, 88]. In the case of 1 torr (Figure 4.2b), while the red-side shoulders have not disappeared, but it could be observed that the 116 and 150 cm^{-1} peaks are relatively sharper than the 1 torr sample baked at 400 °C. The Raman mode at ~225 is affiliated with γ-In_2Se_3 as well [62, 89]. In the case of 2, 3 and 5 torr samples (Figure 4.2c, d and e), the 150 cm^{-1} peaks have become slightly more intense than other shoulders, but they are still present. Finally, When the samples were baked at 600 °C, all broad peaks and shoulders have disappeared in all samples (Figure 4.2a-e), and only the peaks at 116 and 150 were recorded, indicating the transition of the samples to crystallized β and γ-In_2Se_3. In conclusion, the samples are amorphous, and probably multi-phase, In_2Se_3 in the as-deposited case, and once baked at high temperatures, they transform into crystallized β and γ-In_2Se_3.

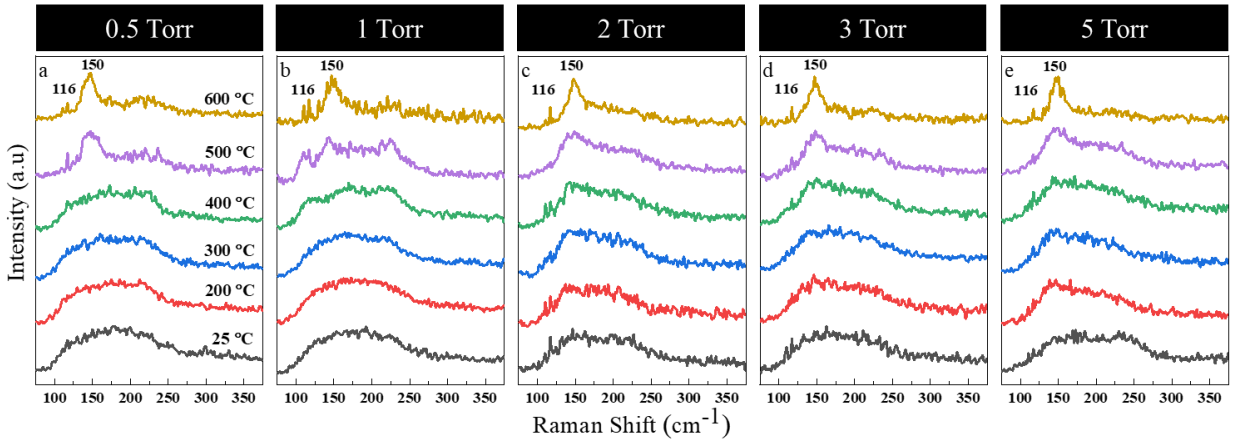

Figure 4.2. Raman spectra showing the effect of baking temperature on the samples deposited at 0.5 (a), 1 (b), 2 (c), 3 (d) and 5 torr (e) background pressures. The samples are amorphous, and probably multi-phase, In_2Se_3 in the as-deposited case, and once baked at high temperatures, they transform into crystallized β and γ-In_2Se_3.

PL spectroscopy was also used to characterize the optical and electronic properties of the obtained In_2Se_3 samples, and again the samples' exposure to the laser has been minimized. First, Figure 4.3a-e is showing the effect of baking temperature on the PL emissions. In general, up to a baking temperature of 400 °C, all samples did not show significant PL emissions. This could be attributed to the lack of crystallinity, as it has been reported that strain relaxation and crystalline defects could act as non-radiative recombination centers and significantly quench the room temperature PL emission [62]. When these samples were heat-treated at 500 °C, slight PL emission enhancement has been observed with a central emission located at ~650 nm. This central emission corresponds to 1.90 eV, which is in the proximity range of γ-In_2Se_3 bandgap [62]. At a baking temperature of 600 °C, all samples have witnessed outstanding PL emission amplification. The PL emission is consisted of a narrow and intense peak located at 650 nm, which corresponds to the γ-In_2Se_3. In addition, this 650 nm peak is close to the reported values of γ-In_2Se_3 nanorods and nanowires PL emissions [90, 91], confirming the presence of nanorod structures. In addition, there is another one broad, less intense peak centered at 800 nm. This peak is within the bandgap range of the β phase [64, 71], recorded in the Raman analyses too. Therefore, most likely this peak is

attributed to the β phase. Also, the recombination of carriers at localized states within the bandgap of γ-In_2Se_3 [62] could additionally contribute to the broad and less intense peaks on the red side of the 650 nm peak.

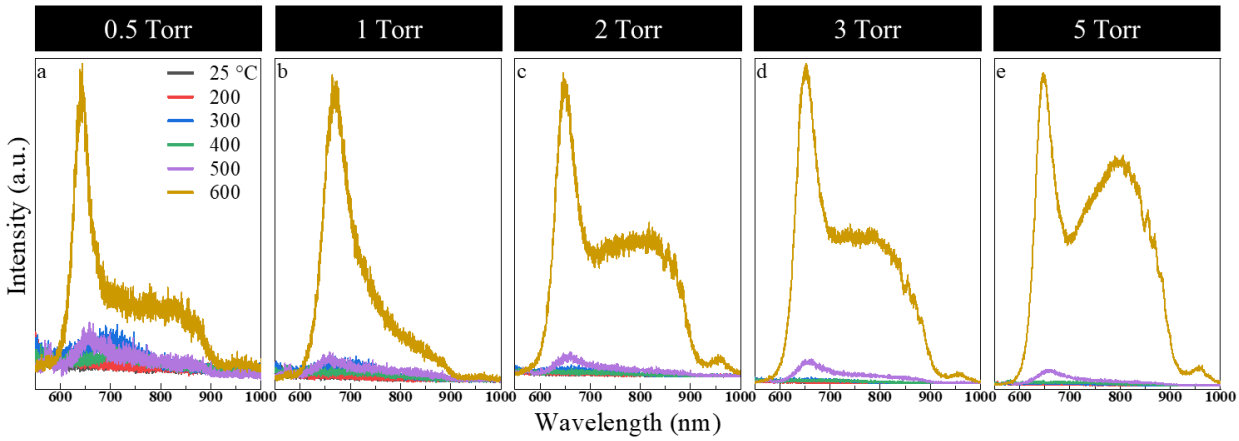

Figure 4.3. PL spectra showing the effect of baking temperature on the samples deposited at 0.5 (a), 1 (b), 2 (c), 3 (d) and 5 torr (e) background pressures. No significant emissions at low temperatures. However, at 600 °C, notable PL enhancements were recorded due to phase transformation and crystallization.

To investigate the correlation between the PL emissions of various pressures, the PL emissions of different pressures are plotted at the indicated temperatures in Figure 4.4a-e. It is seen that up to 400 °C (Figure 3.4a, b and c), no significant PL emissions were detected, and correlations could not be made. At 500 °C (Figure 3.3d), gradual PL enhancements were recorded for all pressures, with intensity positively correlated to deposition background pressures. From our previous experience on GaSe, this could be attributed to the initial plume-induced crystallization at higher pressure. Also, as we know, higher pressure samples sustain high-temperature baking without degradation. At a baking temperature of 600 °C (Figure 3.3e), the PL intensity is increasing as a function of increasing pressure. Again, this could be attributed to the reasons mentioned at 500 °C. Another possible reason could be the high density and quality of the nanorods at higher temperatures.

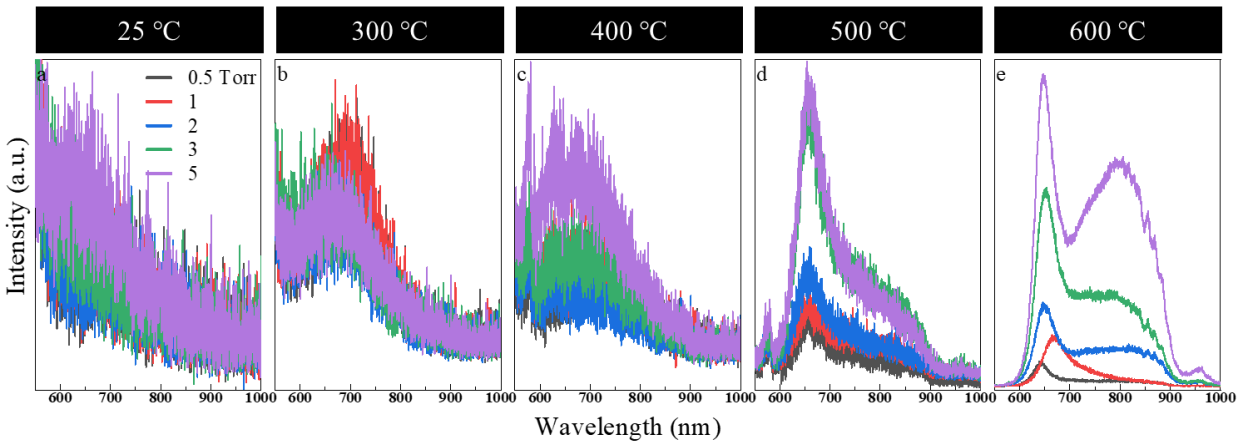

Figure 4.4. PL spectra of the In_2Se_3 deposited at various pressure for the as-deposited case (a) and at the indicated baking temperatures (b–e). The PL emissions are directly correlated to background pressures.

References

[1] Z. Ahmadi, B. Yakupoglu, N. Azam, S. Elafandi, and M. Mahjouri-Samani, "Application of lasers in the synthesis and processing of two-dimensional quantum materials," *Journal of Laser Applications,* vol. 31, no. 3, 2019, doi: 10.2351/1.5100762.

[2] A. Gupta, T. Sakthivel, and S. Seal, "Recent development in 2D materials beyond graphene," *Prog Mater Sci,* vol. 73, pp. 44-126, 2015, doi: 10.1016/j.pmatsci.2015.02.002.

[3] G. R. Bhimanapati *et al.,* "Recent Advances in Two-Dimensional Materials beyond Graphene," *ACS Nano,* vol. 9, no. 12, pp. 11509-11539, 2015, doi: 10.1021/acsnano.5b05556.

[4] X. Wang, G. Sun, N. Li, and P. Chen, "Quantum dots derived from two-dimensional materials and their applications for catalysis and energy," *Chemical Society Reviews,* vol. 45, no. 8, pp. 2239-2262, 2016, doi: 10.1039/c5cs00811e.

[5] M.-R. Gao, Y.-F. Xu, J. Jiang, and S.-H. Yu, "Nanostructured metal chalcogenides: synthesis, modification, and applications in energy conversion and storage devices," *Chemical Society Reviews,* vol. 42, no. 7, 2013, doi: 10.1039/c2cs35310e.

[6] N. Azam *et al.,* "Accelerated synthesis of atomically-thin 2D quantum materials by a novel laser-assisted synthesis technique," *2D Materials,* vol. 7, no. 1, 2019, doi: 10.1088/2053-1583/ab53f7.

[7] Z. Ahmadi, B. Yakupoglu, N. Azam, S. Elafandi, and M. Mahjouri-Samani, "Self-limiting laser crystallization and direct writing of 2D materials," *International Journal of Extreme Manufacturing,* vol. 1, no. 1, 2019, doi: 10.1088/2631-7990/ab0edc.

[8] A. Kumar and P. K. Ahluwalia, "Electronic structure of transition metal dichalcogenides monolayers 1H-MX2 (M = Mo, W; X = S, Se, Te) from ab-initio theory: new direct band gap semiconductors," *The European Physical Journal B,* vol. 85, no. 6, 2012, doi: 10.1140/epjb/e2012-30070-x.

[9] M. G. Stanford *et al.,* "High Conduction Hopping Behavior Induced in Transition Metal Dichalcogenides by Percolating Defect Networks: Toward Atomically Thin Circuits," *Advanced Functional Materials,* vol. 27, no. 36, 2017, doi: 10.1002/adfm.201702829.

[10] L. Ye, H. Li, Z. Chen, and J. Xu, "Near-Infrared Photodetector Based on MoS2/Black Phosphorus Heterojunction," *ACS Photonics,* vol. 3, no. 4, pp. 692-699, 2016, doi: 10.1021/acsphotonics.6b00079.

[11] Q. Fu *et al.,* "Synthesis and Enhanced Electrochemical Catalytic Performance of Monolayer WS2(1-x)Se2xwith a Tunable Band Gap," *Advanced Materials,* vol. 27, no. 32, pp. 4732-4738, 2015, doi: 10.1002/adma.201500368.

[12] N. Morell *et al.*, "High Quality Factor Mechanical Resonators Based on WSe2 Monolayers," *Nano Letters*, vol. 16, no. 8, pp. 5102-5108, 2016, doi: 10.1021/acs.nanolett.6b02038.

[13] M. Chhowalla, H. S. Shin, G. Eda, L.-J. Li, K. P. Loh, and H. Zhang, "The chemistry of two-dimensional layered transition metal dichalcogenide nanosheets," *Nature Chemistry*, vol. 5, no. 4, pp. 263-275, 2013, doi: 10.1038/nchem.1589.

[14] S. Z. Butler *et al.*, "Progress, Challenges, and Opportunities in Two-Dimensional Materials Beyond Graphene," *ACS Nano*, vol. 7, no. 4, pp. 2898-2926, 2013, doi: 10.1021/nn400280c.

[15] S. Ahmed and J. Yi, "Two-Dimensional Transition Metal Dichalcogenides and Their Charge Carrier Mobilities in Field-Effect Transistors," *Nano-Micro Letters*, vol. 9, no. 4, 2017, doi: 10.1007/s40820-017-0152-6.

[16] Q. H. Wang, K. Kalantar-Zadeh, A. Kis, J. N. Coleman, and M. S. Strano, "Electronics and optoelectronics of two-dimensional transition metal dichalcogenides," *Nature Nanotechnology*, vol. 7, no. 11, pp. 699-712, 2012, doi: 10.1038/nnano.2012.193.

[17] S.-H. Bae *et al.*, "Integration of bulk materials with two-dimensional materials for physical coupling and applications," *Nature Materials*, vol. 18, no. 6, pp. 550-560, 2019, doi: 10.1038/s41563-019-0335-2.

[18] S. B. Desai *et al.*, "MoS2 transistors with 1-nanometer gate lengths," *Science*, vol. 354, no. 6308, pp. 99-102, 2016, doi: 10.1126/science.aah4698.

[19] Y. Wang *et al.*, "Cryo-mediated exfoliation and fracturing of layered materials into 2D quantum dots," *Science Advances*, vol. 3, no. 12, 2017, doi: 10.1126/sciadv.1701500.

[20] Y. Liu *et al.*, "Reflux pretreatment-mediated sonication: A new universal route to obtain 2D quantum dots," *Materials Today*, vol. 22, pp. 17-24, 2019, doi: 10.1016/j.mattod.2018.06.007.

[21] H. Huang *et al.*, "Water-Soluble Monolayer Molybdenum Disulfide Quantum Dots with Upconversion Fluorescence," *Particle & Particle Systems Characterization*, vol. 32, no. 1, pp. 72-79, 2015, doi: 10.1002/ppsc.201400101.

[22] B. L. Li *et al.*, "Emerging 0D Transition-Metal Dichalcogenides for Sensors, Biomedicine, and Clean Energy," *Small*, vol. 13, no. 31, 2017, doi: 10.1002/smll.201700527.

[23] Q. Xu *et al.*, "Two-dimensional quantum dots: Fundamentals, photoluminescence mechanism and their energy and environmental applications," *Materials Today Energy*, vol. 10, pp. 222-240, 2018, doi: 10.1016/j.mtener.2018.09.005.

[24] Y. Wang and Y. Ni, "Molybdenum Disulfide Quantum Dots as a Photoluminescence Sensing Platform for 2,4,6-Trinitrophenol Detection," *Analytical Chemistry*, vol. 86, no. 15, pp. 7463-7470, 2014, doi: 10.1021/ac5012014.

[25] W. Gu, Y. Yan, C. Zhang, C. Ding, and Y. Xian, "One-Step Synthesis of Water-Soluble MoS2Quantum Dots via a Hydrothermal Method as a Fluorescent Probe for Hyaluronidase Detection," *ACS Applied Materials & Interfaces,* vol. 8, no. 18, pp. 11272-11279, 2016, doi: 10.1021/acsami.6b01166.

[26] H. Dong *et al.*, "Fluorescent MoS2 Quantum Dots: Ultrasonic Preparation, Up-Conversion and Down-Conversion Bioimaging, and Photodynamic Therapy," *ACS Applied Materials & Interfaces,* vol. 8, no. 5, pp. 3107-3114, 2016, doi: 10.1021/acsami.5b10459.

[27] M. Samadi, N. Sarikhani, M. Zirak, H. Zhang, H.-L. Zhang, and A. Z. Moshfegh, "Group 6 transition metal dichalcogenide nanomaterials: synthesis, applications and future perspectives," *Nanoscale Horizons,* vol. 3, no. 2, pp. 90-204, 2018, doi: 10.1039/c7nh00137a.

[28] L. Yang *et al.*, "Properties, Preparation and Applications of Low Dimensional Transition Metal Dichalcogenides," *Nanomaterials,* vol. 8, no. 7, 2018, doi: 10.3390/nano8070463.

[29] A. Ghorai, S. Bayan, N. Gogurla, A. Midya, and S. K. Ray, "Highly Luminescent WS2 Quantum Dots/ZnO Heterojunctions for Light Emitting Devices," *ACS Applied Materials & Interfaces,* vol. 9, no. 1, pp. 558-565, 2016, doi: 10.1021/acsami.6b12859.

[30] S. Zhang *et al.*, "MoS2 Quantum Dot Growth Induced by S Vacancies in a ZnIn2S4 Monolayer: Atomic-Level Heterostructure for Photocatalytic Hydrogen Production," *ACS Nano,* vol. 12, no. 1, pp. 751-758, 2017, doi: 10.1021/acsnano.7b07974.

[31] X. Ding *et al.*, "Defect engineered bioactive transition metals dichalcogenides quantum dots," *Nature Communications,* vol. 10, no. 1, 2019, doi: 10.1038/s41467-018-07835-1.

[32] S. C. Dhanabalan, B. Dhanabalan, J. S. Ponraj, Q. Bao, and H. Zhang, "2D-Materials-Based Quantum Dots: Gateway Towards Next-Generation Optical Devices," *Advanced Optical Materials,* vol. 5, no. 19, 2017, doi: 10.1002/adom.201700257.

[33] S. Zhang, X. Jia, and E. Wang, "Facile synthesis of optical pH-sensitive molybdenum disulfide quantum dots," *Nanoscale,* vol. 8, no. 33, pp. 15152-15157, 2016, doi: 10.1039/c6nr04726b.

[34] S. P. Caigas *et al.*, "P-Type Doping of WS2 Quantum Dots via Pulsed Laser Ablation," *ACS Photonics,* vol. 5, no. 12, pp. 4828-4837, 2018, doi: 10.1021/acsphotonics.8b00941.

[35] K. H. Ibrahim, M. Irannejad, B. Wales, J. Sanderson, M. Yavuz, and K. P. Musselman, "Simultaneous Fabrication and Functionalization of Nanoparticles of 2D Materials with Hybrid Optical Properties," *Advanced Optical Materials,* vol. 6, no. 11, 2018, doi: 10.1002/adom.201701365.

[36] L. Lin, Y. Xu, S. Zhang, I. M. Ross, A. C. M. Ong, and D. A. Allwood, "Fabrication of Luminescent Monolayered Tungsten Dichalcogenides Quantum Dots with Giant Spin-Valley Coupling," *ACS Nano,* vol. 7, no. 9, pp. 8214-8223, 2013, doi: 10.1021/nn403682r.

[37] D. Vikraman *et al.*, "Direct synthesis of thickness-tunable MoS2 quantum dot thin layers: Optical, structural and electrical properties and their application to hydrogen evolution," *Nano Energy*, vol. 35, pp. 101-114, 2017, doi: 10.1016/j.nanoen.2017.03.031.

[38] D. Gopalakrishnan, D. Damien, and M. M. Shaijumon, "MoS2 Quantum Dot-Interspersed Exfoliated MoS2 Nanosheets," *ACS Nano*, vol. 8, no. 5, pp. 5297-5303, 2014, doi: 10.1021/nn501479e.

[39] V. Štengl and J. Henych, "Strongly luminescent monolayered MoS2 prepared by effective ultrasound exfoliation," *Nanoscale*, vol. 5, no. 8, 2013, doi: 10.1039/c3nr00192j.

[40] Y. Yan, C. Zhang, W. Gu, C. Ding, X. Li, and Y. Xian, "Facile Synthesis of Water-Soluble WS2 Quantum Dots for Turn-On Fluorescent Measurement of Lipoic Acid," *The Journal of Physical Chemistry C*, vol. 120, no. 22, pp. 12170-12177, 2016, doi: 10.1021/acs.jpcc.6b01868.

[41] S. Xu, D. Li, and P. Wu, "One-Pot, Facile, and Versatile Synthesis of Monolayer MoS2/WS2Quantum Dots as Bioimaging Probes and Efficient Electrocatalysts for Hydrogen Evolution Reaction," *Advanced Functional Materials*, vol. 25, no. 7, pp. 1127-1136, 2015, doi: 10.1002/adfm.201403863.

[42] Y. Xu, X. Wang, W. L. Zhang, F. Lv, and S. Guo, "Recent progress in two-dimensional inorganic quantum dots," *Chemical Society Reviews*, vol. 47, no. 2, pp. 586-625, 2018, doi: 10.1039/c7cs00500h.

[43] G. Ou *et al.*, "Defective molybdenum sulfide quantum dots as highly active hydrogen evolution electrocatalysts," *Nano Research*, vol. 11, no. 2, pp. 751-761, 2017, doi: 10.1007/s12274-017-1684-2.

[44] Y. Xu, L. Yan, X. Li, and H. Xu, "Fabrication of transition metal dichalcogenides quantum dots based on femtosecond laser ablation," *Scientific Reports*, vol. 9, no. 1, 2019, doi: 10.1038/s41598-019-38929-5.

[45] B. Li *et al.*, "Preparation of Monolayer MoS2 Quantum Dots using Temporally Shaped Femtosecond Laser Ablation of Bulk MoS2 Targets in Water," *Scientific Reports*, vol. 7, no. 1, 2017, doi: 10.1038/s41598-017-10632-3.

[46] W. Qiao *et al.*, "Luminescent monolayer MoS2 quantum dots produced by multi-exfoliation based on lithium intercalation," *Applied Surface Science*, vol. 359, pp. 130-136, 2015, doi: 10.1016/j.apsusc.2015.10.089.

[47] X. Cao *et al.*, "Transition metal dichalcogenide quantum dots: synthesis, photoluminescence and biological applications," *Journal of Materials Chemistry B*, vol. 6, no. 48, pp. 8011-8036, 2018, doi: 10.1039/c8tb02519c.

[48] X. Zhang, H. Cheng, and H. Zhang, "Recent Progress in the Preparation, Assembly, Transformation, and Applications of Layer-Structured Nanodisks beyond Graphene," *Advanced Materials*, vol. 29, no. 35, 2017, doi: 10.1002/adma.201701704.

[49] D. Gopalakrishnan *et al.*, "Electrochemical synthesis of luminescent MoS2 quantum dots," *Chemical Communications,* vol. 51, no. 29, pp. 6293-6296, 2015, doi: 10.1039/c4cc09826a.

[50] M. O. Valappil, A. Anil, M. Shaijumon, V. K. Pillai, and S. Alwarappan, "A Single-Step Electrochemical Synthesis of Luminescent WS2 Quantum Dots," *Chemistry - A European Journal,* vol. 23, no. 38, pp. 9144-9148, 2017, doi: 10.1002/chem.201701277.

[51] M. Mahjouri-Samani *et al.*, "Nonequilibrium Synthesis of TiO2 Nanoparticle "Building Blocks" for Crystal Growth by Sequential Attachment in Pulsed Laser Deposition," *Nano Letters,* vol. 17, no. 8, pp. 4624-4633, 2017, doi: 10.1021/acs.nanolett.7b01047.

[52] M. Mahjouri-Samani *et al.*, "Digital Transfer Growth of Patterned 2D Metal Chalcogenides by Confined Nanoparticle Evaporation," *ACS Nano,* vol. 8, no. 11, pp. 11567-11575, 2014, doi: 10.1021/nn5048124.

[53] Q. Dai, J. Chen, L. Lu, J. Tang, and W. Wang, "Pulsed Laser Deposition of CdSe Quantum Dots on Zn2SnO4 Nanowires and Their Photovoltaic Applications," *Nano Letters,* vol. 12, no. 8, pp. 4187-4193, 2012, doi: 10.1021/nl301761w.

[54] M. Mahjouri-Samani *et al.*, "Pulsed Laser Deposition of Photoresponsive Two-Dimensional GaSe Nanosheet Networks," *Advanced Functional Materials,* vol. 24, no. 40, pp. 6365-6371, 2014, doi: 10.1002/adfm.201401440.

[55] S. Elafandi, Z. Ahmadi, N. Azam, and M. Mahjouri-Samani, "Gas-Phase Formation of Highly Luminescent 2D GaSe Nanoparticle Ensembles in a Nonequilibrium Laser Ablation Process," *Nanomaterials,* vol. 10, no. 5, 2020, doi: 10.3390/nano10050908.

[56] S. L. Stoll, E. G. Gillan, and A. R. Barron, "Chemical vapor deposition of Gallium selenide and indium selenide nanoparticles," *Chemical Vapor Deposition,* vol. 2, no. 5, pp. 182-184, 1996, doi: 10.1002/cvde.19960020506.

[57] K. Allakhverdiev, J. Hagen, and Z. Salaeva, "On a Possibility to Form Small Crystallites of Layered Gallium Selenide via Ultrasonic Treatment," *physica status solidi (a),* vol. 163, no. 1, pp. 121-127, 1997, doi: 10.1002/1521-396x(199709)163:1<121::Aid-pssa121>3.0.Co;2-k.

[58] V. Chikan and D. F. Kelley, "Synthesis of Highly Luminescent GaSe Nanoparticles," *Nano Letters,* vol. 2, no. 2, pp. 141-145, 2002, doi: 10.1021/nl015641m.

[59] P. Fassl *et al.*, "Effect of density of surface defects on photoluminescence properties in MAPbI3 perovskite films," *Journal of Materials Chemistry C,* vol. 7, no. 18, pp. 5285-5292, 2019, doi: 10.1039/c8tc05998e.

[60] L. Liu *et al.*, "Atomically Resolving Polymorphs and Crystal Structures of In2Se3," *Chemistry of Materials,* vol. 31, no. 24, pp. 10143-10149, 2019, doi: 10.1021/acs.chemmater.9b03499.

[61] C.-H. Ho, "Amorphous effect on the advancing of wide-range absorption and structural-phase transition in γ-In2Se3 polycrystalline layers," *Scientific Reports,* vol. 4, no. 1, 2014, doi: 10.1038/srep04764.

[62] N. Balakrishnan *et al.*, "Epitaxial growth of γ -InSe and α, β, and γ -In2Se3 on ε -GaSe," *2D Materials,* vol. 5, no. 3, 2018, doi: 10.1088/2053-1583/aac479.

[63] X. Wei *et al.*, "Synthesis of tetragonal prismatic γ-In2Se3 nanostructures with predominantly {110} facets and photocatalytic degradation of tetracycline," *Applied Catalysis B: Environmental,* vol. 260, 2020, doi: 10.1016/j.apcatb.2019.118218.

[64] N. Balakrishnan *et al.*, "Quantum confinement and photoresponsivity of β-In2Se3 nanosheets grown by physical vapour transport," *2D Materials,* vol. 3, no. 2, 2016, doi: 10.1088/2053-1583/3/2/025030.

[65] J. Zhou *et al.*, "Controlled Synthesis of High-Quality Monolayered α-In2Se3 via Physical Vapor Deposition," *Nano Letters,* vol. 15, no. 10, pp. 6400-6405, 2015, doi: 10.1021/acs.nanolett.5b01590.

[66] T. Li *et al.*, "Multi-morphological growth of nano-structured In2Se3 by ambient pressure triethylene glycol based solution syntheses," *Journal of Alloys and Compounds,* vol. 646, pp. 603-611, 2015, doi: 10.1016/j.jallcom.2015.05.193.

[67] J. Quereda, R. Biele, G. Rubio-Bollinger, N. Agraït, R. D'Agosta, and A. Castellanos-Gomez, "Strong Quantum Confinement Effect in the Optical Properties of Ultrathin α-In2Se3," *Advanced Optical Materials,* vol. 4, no. 12, pp. 1939-1943, 2016, doi: 10.1002/adom.201600365.

[68] R. B. Jacobs-Gedrim *et al.*, "Extraordinary Photoresponse in Two-Dimensional In2Se3 Nanosheets," *ACS Nano,* vol. 8, no. 1, pp. 514-521, 2013, doi: 10.1021/nn405037s.

[69] G. Mohan Kumar *et al.*, "Photoelectrochemical analysis of shape modified γ- phase In2Se3 nanostructures photoelectrodes," *Journal of Materials Research and Technology,* vol. 9, no. 6, pp. 12318-12327, 2020, doi: 10.1016/j.jmrt.2020.08.092.

[70] P. K. Mohapatra, K. Ranganathan, L. Dezanashvili, L. Houben, and A. Ismach, "Epitaxial growth of In2Se3 on monolayer transition metal dichalcogenide single crystals for high performance photodetectors," *Applied Materials Today,* vol. 20, 2020, doi: 10.1016/j.apmt.2020.100734.

[71] Z. Zou *et al.*, "Epitaxial synthesis of ultrathin β-In2Se3/MoS2 heterostructures with high visible/near-infrared photoresponse," *Nanoscale,* vol. 12, no. 11, pp. 6480-6488, 2020, doi: 10.1039/c9nr10387b.

[72] S. Dhongade, P. R. Mutadak, A. B. Deore, M. A. More, A. Furube, and P. Koinkar, "In2Se3 Nanocubes as High Current Density Cold Cathode Materials," *ACS Applied Nano Materials,* vol. 3, no. 10, pp. 9749-9758, 2020, doi: 10.1021/acsanm.0c01844.

[73] W. Ding *et al.*, "Prediction of intrinsic two-dimensional ferroelectrics in In2Se3 and other III2-VI3 van der Waals materials," *Nature Communications*, vol. 8, no. 1, 2017, doi: 10.1038/ncomms14956.

[74] Y. Zhou *et al.*, "Out-of-Plane Piezoelectricity and Ferroelectricity in Layered α-In2Se3 Nanoflakes," *Nano Letters*, vol. 17, no. 9, pp. 5508-5513, 2017, doi: 10.1021/acs.nanolett.7b02198.

[75] T. Zhai *et al.*, "Fabrication of High-Quality In2Se3 Nanowire Arrays toward High-Performance Visible-Light Photodetectors," *ACS Nano*, vol. 4, no. 3, pp. 1596-1602, 2010, doi: 10.1021/nn9012466.

[76] Y.-J. Hsiao, C.-H. Lu, L.-W. Ji, T.-H. Meen, Y.-L. Chen, and H.-P. Chi, "Characterization of photovoltaics with In2S3 nanoflakes/p-Si heterojunction," *Nanoscale Research Letters*, vol. 9, no. 1, 2014, doi: 10.1186/1556-276x-9-32.

[77] H. Lee, D.-H. Kang, and L. Tran, "Indium selenide (In2Se3) thin film for phase-change memory," *Materials Science and Engineering: B*, vol. 119, no. 2, pp. 196-201, 2005, doi: 10.1016/j.mseb.2005.02.060.

[78] J. L. Collins *et al.*, "Electronic Band Structure of In-Plane Ferroelectric van der Waals β′-In2Se3," *ACS Applied Electronic Materials*, vol. 2, no. 1, pp. 213-219, 2020, doi: 10.1021/acsaelm.9b00699.

[79] C. Julien, E. Hatzikraniotis, A. Chevy, and K. Kambas, "Electrical behavior of lithium intercalated layered In-Se compounds," *Materials Research Bulletin*, vol. 20, no. 3, pp. 287-292, 1985, doi: 10.1016/0025-5408(85)90185-0.

[80] X. Tan, J. Zhou, and Q. Yang, "Ascorbic acid-assisted solvothermal growth of γ-In2Se3 hierarchical flowerlike architectures," *CrystEngComm*, vol. 13, no. 7, 2011, doi: 10.1039/c0ce00790k.

[81] S. N. Malik, H. Ahmed, M. Shahid, N. Haider, M. A. Malik, and P. O'Brien, "Colloidal preparation of copper selenide and indium selenide nanoparticles by single source precursors approach," presented at the Proceedings of 2013 10th International Bhurban Conference on Applied Sciences & Technology (IBCAST), 2013.

[82] P. Liu, S. Yu, W. Fan, and W. Shi, "A new inorganic–organic hybrid In2Se3(en) as hollow nanospheres: hydrothermal synthesis and near-infrared photoluminescence properties," *Dalton Transactions*, vol. 42, no. 8, 2013, doi: 10.1039/c2dt32589f.

[83] W. Shi, S. Yu, P. Liu, W. Fan, H. Luo, and S. Song, "Near-infrared photoluminescent flowerlike α-In2Se3 nanostructures from a solvothermal treatment," *Chemical Engineering Journal*, vol. 225, pp. 474-480, 2013, doi: 10.1016/j.cej.2013.03.066.

[84] V. D. Botcha *et al.*, "Growth and thermal properties of various In2Se3 nanostructures prepared by single step PVD technique," *Journal of Alloys and Compounds*, vol. 773, pp. 698-705, 2019, doi: 10.1016/j.jallcom.2018.09.335.

[85] C. H. d. Groot and J. S. Moodera, "Growth and characterization of a novel In2Se3 structure," *Journal of Applied Physics,* vol. 89, no. 8, pp. 4336-4340, 2001, doi: 10.1063/1.1355287.

[86] P. Reyes-Figueroa *et al.,* "Structural properties of In2Se3 precursor layers deposited by spray pyrolysis and physical vapor deposition for CuInSe2 thin-film solar cell applications," *Thin Solid Films,* vol. 587, pp. 112-116, 2015, doi: 10.1016/j.tsf.2015.01.035.

[87] J. Igo, M. Gabel, Z.-G. Yu, L. Yang, and Y. Gu, "Photodefined In-Plane Heterostructures in Two-Dimensional In2Se3 Nanolayers for Ultrathin Photodiodes," *ACS Applied Nano Materials,* vol. 2, no. 10, pp. 6774-6782, 2019, doi: 10.1021/acsanm.9b01745.

[88] S. Li *et al.,* "Substrate-induced phase control of In2Se3 thin films," *Journal of Alloys and Compounds,* vol. 845, 2020, doi: 10.1016/j.jallcom.2020.156270.

[89] D. Y. Lyu *et al.,* "Structural and optical characterization of single-phase γ-In2Se3 films with room-temperature photoluminescence," *Journal of Alloys and Compounds,* vol. 499, no. 1, pp. 104-107, 2010, doi: 10.1016/j.jallcom.2010.03.130.

[90] M. D. Yang *et al.,* "Structural and Optical Characteristics ofγ-In2Se3Nanorods Grown on Si Substrates," *Journal of Nanomaterials,* vol. 2011, pp. 1-5, 2011, doi: 10.1155/2011/976262.

[91] M. D. Yang *et al.,* "Hot Photoluminescence in γ-In2Se3 Nanorods," *Nanoscale Research Letters,* vol. 3, no. 11, pp. 427-430, 2008, doi: 10.1007/s11671-008-9173-x.

Appendix A

Supplementary Data of GaSe Nanoparticles

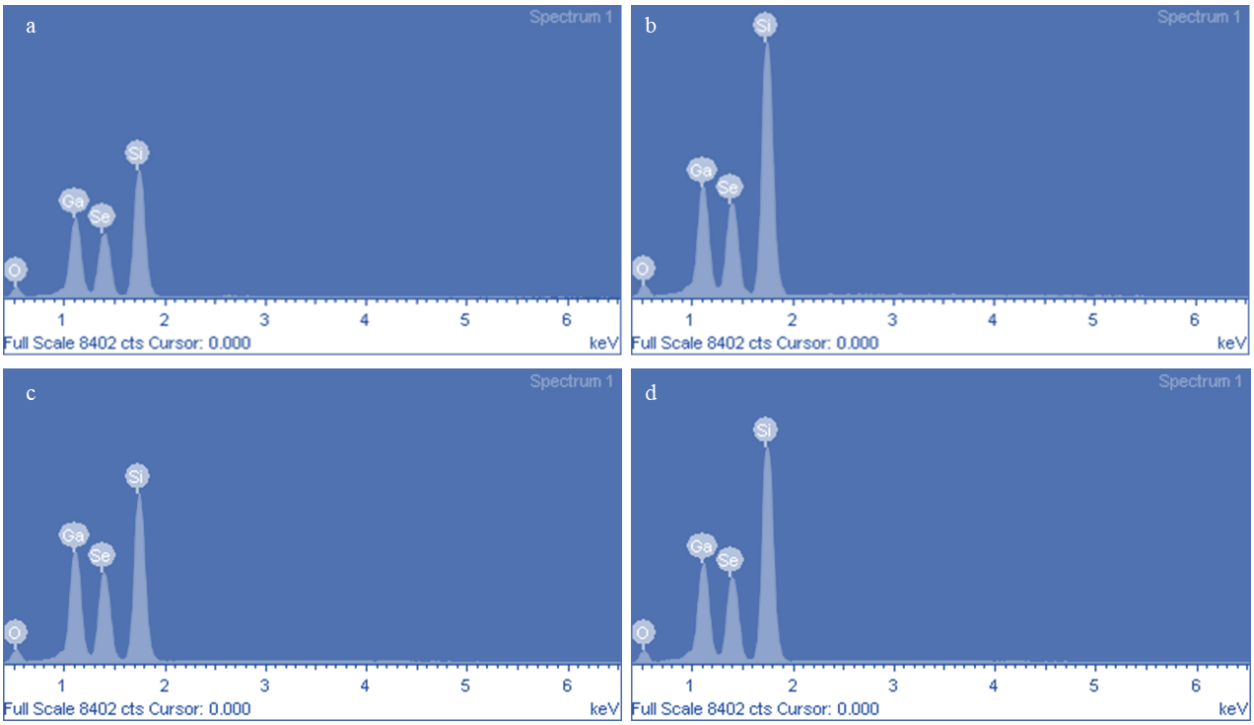

Figure A.1. Energy Dispersive X-ray (EDX) results showing the stoichiometry of the as-deposited nanoparticles at 2 torr (**a**) and 5 torr (**b**) background pressures. The results verify that the stoichiometry is maintained even after baking the sample at 400ºC (**c,d**).

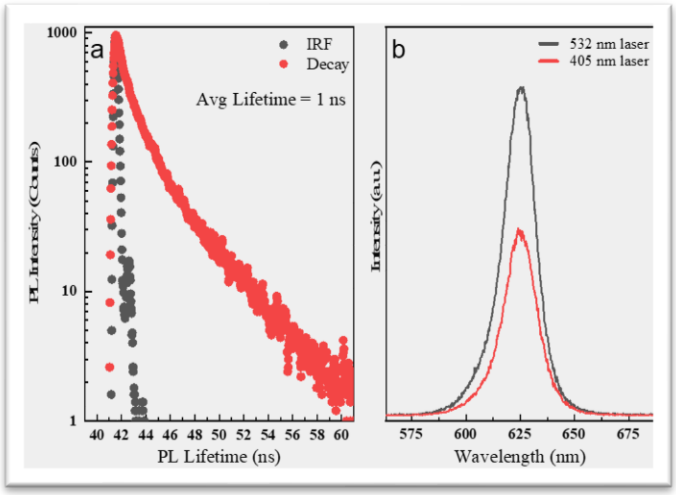

Figure A.2. PL lifetime (a) and PL (b) of GaSe bulk crystal.

Table A.1. Central emission values of the PL emission obtained using the picosecond 405 nm laser as an excitation source.

Pressure	Central Emission (nm)	Central Emission (nm)	Central Emission (nm)	Central Emission (nm)	Central Emission (nm)
Temp (°C)	25°C	200°C	300°C	400°C	500°C
0.5	546	549	601	536	546
1	541	541	614	619	547
2	539	539	552	612	630
3	539	544	543	612	631
5	542	548	547	570	674

Table A.2. FWHM values of the PL emission obtained using the picosecond 405 nm laser as an excitation source.

Pressure	FWHM (nm)	FWHM (nm)	FWHM (nm)	FWHM (nm)	FWHM (nm)
Temp (°C)	25°C	200°C	300°C	400°C	500°C
0.5	129	142.1	208	119	123
1	110	111	233	227	130
2	109	118	144	226	235
3	112	119	116	219	235
5	111	120	116	189	257

Table A.3. Lifetime fitting parameters of the nanoparticles deposited at 0.5 torr.

	˚C	A	T1 (ns)	T2 (ns)	T3 (ns)	B1	B2	B3	Avg T (ns)
0.5 Torr	25	0.3765	0.731225	0.129307	3.627073	0.033445	0.205506	0.003596	0.264171
	200	0.30215	0.588688	3.41839	0.091332	0.032011	0.003651	0.290323	0.177437
	300	0.184215	0.078943	0.478933	2.884721	0.36545	0.024806	0.0011	0.112183
	400	0.465397	0.725004	4.066824	0.090214	0.027162	0.004158	0.298196	0.192724
	500	0.63646	0.410023	0.059662	2.369051	0.030851	0.442596	0.003301	0.098325

Table A.4. Lifetime fitting parameters of the nanoparticles deposited at 1 torr.

	˚C	A	T1 (ns)	T2 (ns)	T3 (ns)	B1	B2	B3	Avg T (ns)
1 Torr	25	0.4274271	0.7540962	0.1585956	3.2313438	0.032112	0.1708399	0.0042126	0.313385
	200	0.3543137	0.7101392	4.3855397	0.1132297	0.0383503	0.0065988	0.2031747	0.31911
	300	0.2901749	0.5743158	0.1017695	2.5332397	0.0242911	0.289314	0.0017508	0.151668
	400	0.3237967	0.5250072	0.0906471	2.1481171	0.0330297	0.3004887	0.0032448	0.153074
	500	0.6234256	0.3056314	1.901737	0.0334506	0.0401633	0.0030453	0.9745709	0.0497813

Table A.5. Lifetime fitting parameters of the nanoparticles deposited at 2 torr.

	˚C	A	T1 (ns)	T2 (ns)	T3 (ns)	B1	B2	B3	Avg T (ns)
2 Torr	25	0.1750575	0.8592292	4.024655	0.1634982	0.0361958	0.0050445	0.1581142	0.387522
	200	0.4279814	0.6497374	0.1295084	3.0860115	0.040692	0.1824145	0.0052144	0.289746
	300	0.4761335	0.6633929	0.1328094	2.8366252	0.0391765	0.1749509	0.0059546	0.300413
	400	0.3829398	0.5212455	0.120366	1.9983458	0.0483285	0.1789817	0.0083602	0.269193
	500	0.3363721	0.4745001	0.0835505	2.0378402	0.0377126	0.3200647	0.0025176	0.138127

Table A.6. Lifetime fitting parameters of the nanoparticles deposited at 3 torr.

	˚C	A	T1 (ns)	T2 (ns)	T3 (ns)	B1	B2	B3	Avg T (ns)
3 Torr	25	0.2446444	0.8186526	0.1679898	3.5211749	0.0320765	0.1575633	0.0032469	0.332638
	200	0.2543762	0.155196	0.7887412	3.6735355	0.1481988	0.0402304	0.0041208	0.362862
	300	0.3710518	0.7357355	0.1141849	4.3359261	0.0444039	0.1743323	0.0077847	0.38111
	400	0.4775388	0.7273778	2.7051167	0.1533387	0.0414428	0.0063572	0.1465101	0.359257
	500	0.5027549	0.4406089	2.1853672	0.0809183	0.0506979	0.0058303	0.2861599	0.169936

Table A.7. Lifetime fitting parameters of the nanoparticles deposited at 5 torr.

	˚C	A	T1 (ns)	T2 (ns)	T3 (ns)	B1	B2	B3	Avg T (ns)
5 Torr	25	0.2624931	0.7419071	0.1670818	3.2860058	0.0396093	0.1460485	0.0054006	0.374413
	200	0.3642784	0.7089714	0.1346335	2.8893663	0.0364951	0.1959548	0.0036873	0.266413
	300	0.4108882	0.7462776	4.1229113	0.1276789	0.0438383	0.0076454	0.1691439	0.389039
	400	0.3218829	0.7118832	2.9545632	0.1211159	0.046988	0.0070916	0.1756727	0.329395
	500	0.2602637	0.0923414	0.5211756	1.8048778	0.2468006	0.0406756	0.0043775	0.177794